Fungal biofilm architecture produces hypoxic microenvironments that drive antifungal resistance

Caitlin H. Kowalski[a], Kaesi A. Morelli[a], Daniel Schultz[a], Carey D. Nadell[b], and Robert A. Cramer[a,1]

[a]Department of Microbiology and Immunology, Geisel School of Medicine at Dartmouth, Hanover, NH 03755; and [b]Department of Biological Sciences, Dartmouth College, Hanover, NH 03755

Edited by Dianne K. Newman, California Institute of Technology, Pasadena, CA, and approved August 6, 2020 (received for review February 26, 2020)

Human fungal infections may fail to respond to contemporary antifungal therapies in vivo despite in vitro fungal isolate drug susceptibility. Such a discrepancy between in vitro antimicrobial susceptibility and in vivo treatment outcomes is partially explained by microbes adopting a drug-resistant biofilm mode of growth during infection. The filamentous fungal pathogen *Aspergillus fumigatus* forms biofilms in vivo, and during biofilm growth it has reduced susceptibility to all three classes of contemporary antifungal drugs. Specific features of filamentous fungal biofilms that drive antifungal drug resistance remain largely unknown. In this study, we applied a fluorescence microscopy approach coupled with transcriptional bioreporters to define spatial and temporal oxygen gradients and single-cell metabolic activity within *A. fumigatus* biofilms. Oxygen gradients inevitably arise during *A. fumigatus* biofilm maturation and are both critical for, and the result of, *A. fumigatus* late-stage biofilm architecture. We observe that these self-induced hypoxic microenvironments not only contribute to filamentous fungal biofilm maturation but also drive resistance to antifungal treatment. Decreasing oxygen levels toward the base of *A. fumigatus* biofilms increases antifungal drug resistance. Our results define a previously unknown mechanistic link between filamentous fungal biofilm physiology and contemporary antifungal drug resistance. Moreover, we demonstrate that drug resistance mediated by dynamic oxygen gradients, found in many bacterial biofilms, also extends to the fungal kingdom. The conservation of hypoxic drug-resistant niches in bacterial and fungal biofilms is thus a promising target for improving antimicrobial therapy efficacy.

hypoxia | antifungals | drug resistance | *Aspergillus fumigatus* | oxygen

The spread of antimicrobial drug resistance resulting from genetically encoded, heritable mechanisms is a global issue for both prokaryotic and eukaryotic pathogens (1, 2). Drug-resistant microbial isolates are clinically defined by standardized metrics, such as minimum inhibitory (MIC) or minimum effective concentrations, through microdilution assays with planktonic cultures (3). However, infection treatment failures still occur with clinically determined, drug-susceptible isolates (4–9). The biofilm mode of growth has been shown to facilitate antimicrobial drug resistance for bacteria (10, 11), yeast (12–15), and filamentous fungi (16, 17) and is likely a contributing factor to the discrepancy between MIC data and clinical outcomes. Biofilm characteristics such as extracellular matrix (ECM) production (18–21), elevated efflux pump activity (22–26), and altered metabolic states (27, 28) have been described, among others, to contribute to bacterial and fungal biofilm antimicrobial drug resistance. Yet, investigation of the spatial and functional features of morphologically diverse yeast and filamentous fungal biofilms, and their relationship to antifungal drug resistance, remains a significant gap in knowledge (29).

Specific features of filamentous fungal biofilms may be unique to their biology and drive antimicrobial drug resistance. For example, filamentous fungal biofilms are characterized by a network of filaments, or hyphae, which form large spaces between cells which may allow mass transfer of nutrients. Intriguingly, strains of the human fungal pathogen *Aspergillus fumigatus* with more abundant growth under low-oxygen conditions have altered biofilm morphology, suggesting oxygen dynamics within filamentous fungal biofilms may affect biofilm function and maturation (30). While low-oxygen environments are now considered a canonical feature of many bacterial and yeast biofilms, whether obligate aerobic filamentous fungi form such environments in their biofilms and whether they impact fungal responses to stress are ill-defined (31–39). To address these gaps in knowledge, we applied high-resolution fluorescence microscopy to visualize filamentous fungal biofilm maturation and coupled this approach with fluorescent bioreporter systems, microelectrode-based oxygen detection, and computational modeling to spatially define oxygen-limited (hypoxic) microenvironments and reduced metabolic activity within mature *A. fumigatus* biofilms. Through these methods we observe that despite the abundant space between hyphae within a filamentous fungal biofilm, hypoxic zones result from self-induced fungal mitochondrial oxygen consumption. In contrast to the ECM-mediated drug resistance of yeast biofilms, we observe that the self-induced physiological hypoxia ultimately facilitates filamentous fungal cell survival in the presence of high-dose antifungals (40). Taken together, these data suggest that hypoxic microenvironments are intrinsic to filamentous fungal biofilms and facilitate fungal survival in the face of contemporary antifungal therapies.

Significance

Failure of antimicrobial therapies to clear an infection is in part due to a biofilm mode of bacterial and fungal growth. Understanding how microbial biofilms mediate antimicrobial treatment failure is critical for improving infection outcomes. The mechanisms by which filamentous fungal biofilms mediate drug resistance are particularly ill-defined. We observe that *Aspergillus fumigatus* biofilms develop hypoxic microenvironments during maturation that facilitate fungal survival in the face of antifungal treatments. Oxygenation of *A. fumigatus* biofilms, however, reduces fungal survival. These results extend the role of dynamic biofilm oxygen gradients found in bacterial pathogens to the fungal kingdom and provide insights into how to overcome fungal drug resistance through manipulation of biofilm oxygen availability and consumption.

Author contributions: C.H.K. and R.A.C. designed research; C.H.K., K.A.M., D.S., and C.D.N. performed research; C.H.K., K.A.M., D.S., and C.D.N. contributed new reagents/analytic tools; C.H.K., K.A.M., D.S., C.D.N., and R.A.C. analyzed data; C.H.K., C.D.N., and R.A.C. wrote the paper; and R.A.C. supervised the research.

The authors declare no competing interest.

This article is a PNAS Direct Submission.

[1]To whom correspondence may be addressed. Email: Robert.A.Cramer.Jr@dartmouth.edu.

This article contains supporting information online at https://www.pnas.org/lookup/suppl/doi:10.1073/pnas.2003700117/-/DCSupplemental.

First published August 26, 2020.

Results

Geometry of Oxygen Availability Governs *A. fumigatus* Biofilm Architecture. To identify filamentous fungal biofilm features that impact antifungal drug resistance, we first explored the impact of oxygen availability on biofilm maturation. Our previous work described oxygen-dependent changes in *A. fumigatus* biofilm morphology between atmospheric (~21%, normoxia) and low-oxygen (0.2%, hypoxia) conditions (30). This change in architecture, measured as the degree to which hyphae deviate from the axis orthogonal to their base coverslip, increases gradually with a reduction in macroenvironment oxygen tension (Fig. 1 *A* and *B*). The overall biomass density within the biofilm does not decrease until biofilms are cultured at 2% O_2 (Fig. 1*C*). Biomass distribution is not altered until the biofilms are cultured at 0.2% O_2, where biomass localizes completely at the air–liquid interface (Fig. 1*C*). The inability of the biomass to grow at the coverslip at 0.2% oxygen suggests that oxygen tensions become growth-limiting near the coverslip in this low-oxygen environment. Notably, the binary switch from growth at the coverslip in atmospheric oxygen to growth at the interface at 0.2% O_2 is observed in other filamentous fungi including a second strain of *A. fumigatus* CEA10, a close relative, *Aspergillus nidulans*, and an evolutionarily distant relative, *Scedosporium apiospermum* (*SI Appendix*, Fig. S1). In support of this interpretation, growth of the fungus at 0.2% O_2 on an oxygen-permeable plate restores growth at the coverslip (Fig. 1*A*). Taken together, these data suggest that dynamic oxygen tensions have an important role in shaping filamentous fungal biofilm maturation.

Given the increased growth under oxygen-limiting conditions on an oxygen-permeable plate, we hypothesize that the vertical hyphae formation characteristic of standard laboratory-condition biofilms (in atmospheric oxygen) is driven by a reduction in oxygen tension as the biofilm matures. In support of this hypothesis, growth on oxygen-permeable plates in atmospheric conditions yields a late-stage 24-h biofilm that is largely devoid of vertically aligned hyphae growing toward the air–liquid interface; instead, we observed biofilms with dense hyphal mats directly on and aligned with the permeable surface (Fig. 1*D*). Together these data indicate that the interaction of hyphal cell growth with local oxygen gradients strongly determines the final architecture of filamentous fungal biofilms, and that this is dependent on the geometry of the surface relative to the source of oxygen. Moreover, these data raise the intriguing hypothesis that hypoxic microenvironments within the filamentous fungal biofilm arise and impact biofilm form and function.

Adaptation to Hypoxic Microenvironments in the Biofilm Contributes to *A. fumigatus* Biofilm Maturation. To test for the presence hypoxic zones within mature filamentous fungal biofilms, we measured dissolved oxygen using microelectrodes within submerged fungal biofilms from inoculation (time = 0 h) to maturity (time = 36 h) (Fig. 2*A*). At a depth from the air–liquid interface of 2.5 mm, dissolved oxygen gradually and significantly decreases as the biofilm matures (Fig. 2*B*). A limitation of the microelectrode is that oxygen cannot be measured directly at the coverslip. To circumvent this, we applied two independent approaches. First, we measured biomass accumulation and distribution over time (*SI Appendix*, Fig. S2) to parameterize a reaction–diffusion model of biofilm development and oxygen tensions (*SI Appendix*, Fig. S3). These data, combined with the oxygen measurements above the biomass (Fig. 2*A*) and published rates of *A. fumigatus* oxygen consumption at ambient and low oxygen (41), were used to generate models to calculate oxygen tensions further into the biofilm. These models robustly predict the emergence of stratified zones of normoxia (<5% O_2), hypoxia (5% > O_2 > 0), and anoxia (0% O_2) within the developing biofilm (Fig. 2*C* and *SI Appendix*, Fig. S4), with hypoxic zones beginning to develop between 14 h and 16 h when cultured under ambient oxygen conditions (~21% O_2).

If hypoxic microenvironments indeed arise early in filamentous fungal biofilm development and contribute to verticalized growth of hyphal filaments, we reasoned that null mutants of genes critical for the *A. fumigatus* hypoxia response would fail to form this characteristic architecture. The mutant strain Δ*srbB* is able to grow in low oxygen, but with a ~50% growth reduction in liquid batch cultures (42). A 24-h biofilm with Δ*srbB* grown at ambient oxygen (21% O2) is stunted with a clear reduction in overall biomass and vertical growth (Fig. 2*D*). Additionally, a mutant completely unable to grow in low-oxygen conditions, Δ*srbA* (43), fails to develop a mature biofilm with vertically aligned hyphal growth by 24 h in two independent strain backgrounds when grown at ambient oxygen (Fig. 2*D*). Conversely,

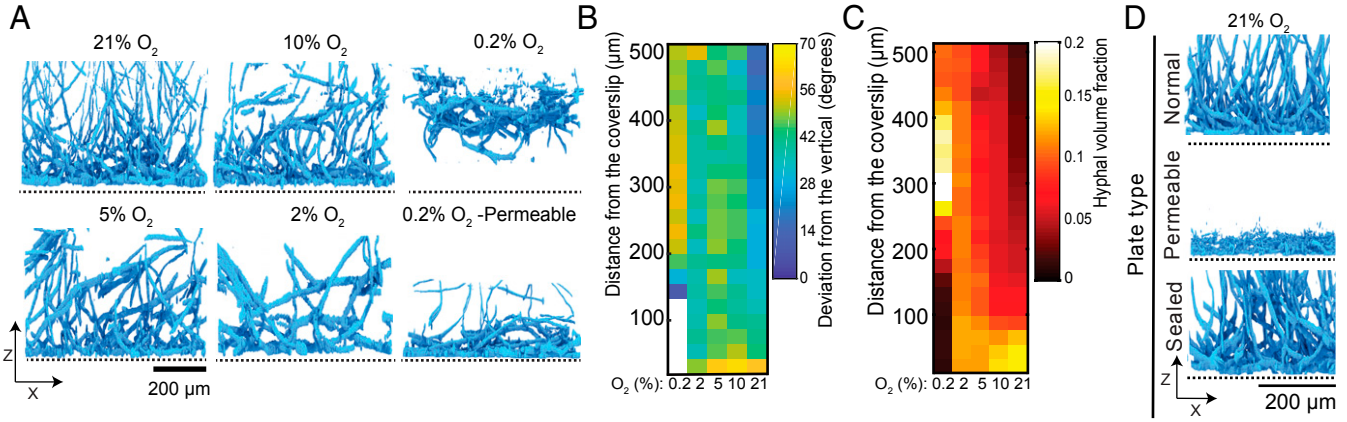

Fig. 1. Oxygen gradients within submerged fungal biofilms are necessary for maturation. (*A*) Representative 3D renderings from $n = 3$ independent biological samples depicting the side view (XZ) of mature biofilms cultured at various oxygen tensions on normal and oxygen-permeable plates. (Scale bar, 200 μm.) (*B*) Heat map illustrating the alteration in hyphal architecture within biofilms cultured on normal plates as a result of reduced oxygen tensions, where architecture is defined as the angle hyphae deviate from a vertical axis. Each column is representative of $n = 3$ independent biological samples. (*C*) Heat map illustrating the altered distribution of fungal biomass as a function of height in biofilms at various oxygen tensions, as shown in *A*. Each column is representative of $n = 3$ independent biological samples. (*D*) Representative 3D renderings of 24-h biofilms from $n = 3$ independent biological samples have a collapsed architecture when cultured on an oxygen permeable surface and sealing of the surface with an oxygen-impermeable seal restores the normal plate architecture. (Scale bar, 200 μm.)

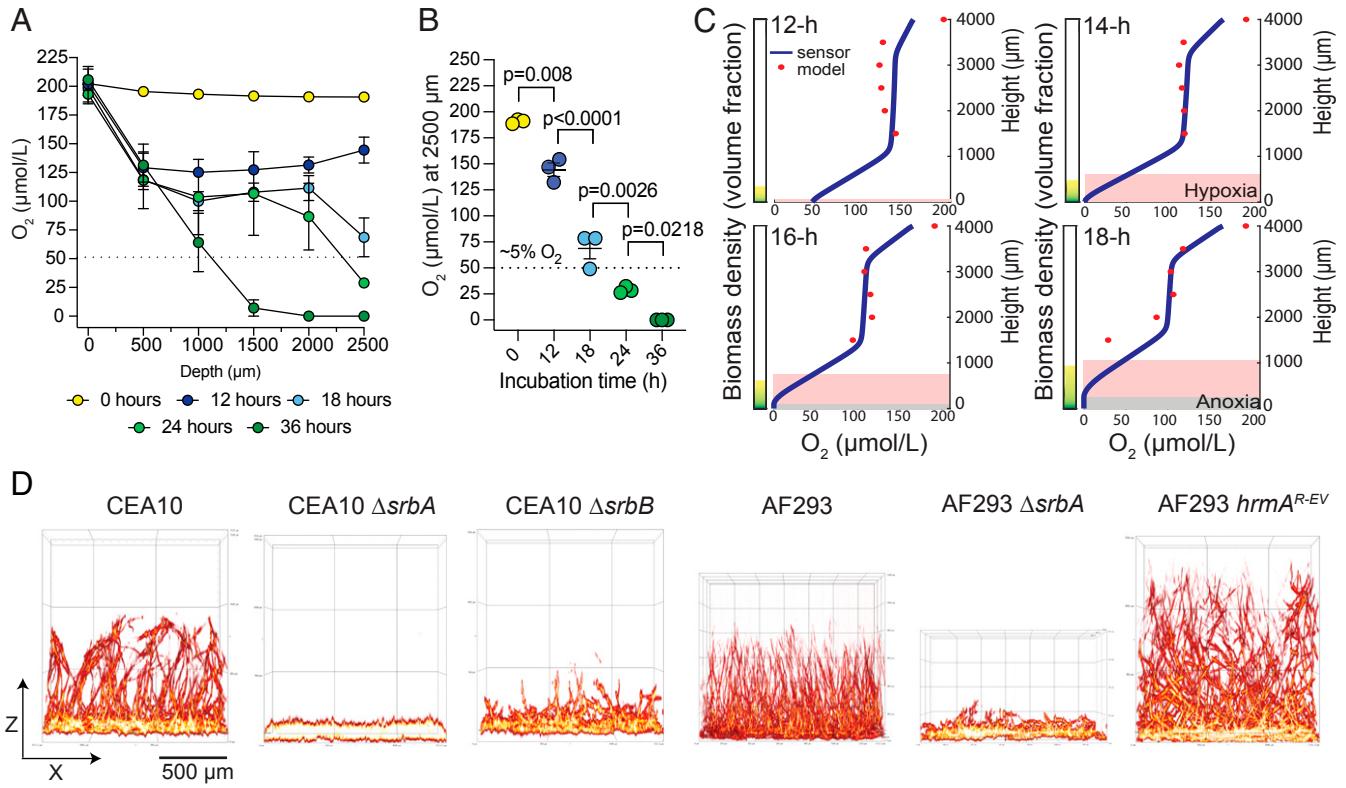

Fig. 2. Hypoxia occurs during maturation of *A. fumigatus* biofilms. (*A*) Measurements of dissolved oxygen within developing fungal biofilms from $n = 3$ independent biological samples. Error bars depict SEM. (*B*) Extrapolation from data in *A* at 2,500 μm depth shows oxygen tensions gradually and significantly reduce throughout biofilm maturation. Error bars indicate SEM of $n = 3$ independent biological samples (one-way ANOVA with Tukey's multiple comparisons test). (*C*) Computational modeling of oxygen zones within a fungal biofilm as a function of oxygen consumption and biomass. White zone: $5\% < O_2 \leq 21\%$, red/hypoxic zone: $0\% < O_2 \leq 5\%$, gray/anoxic zone: $O_2 = 0\%$. (*D*) Representative images ($n = 3$ independent biological samples) of mutant strains of *A. fumigatus* with partial (CEA10 Δ*srbB*) or absolute (CEA10 Δ*srbA*; AF293 Δ*srbA*) low-oxygen growth defects form stunted 24-h biofilms in normoxia. The hypoxia-fit strain $hrmA^{R\text{-}EV}$ forms a more robust 24-h biofilm compared to the control AF293 (representative of $n = 3$ independent biological samples). (Scale bar, 500 μm.)

expression of an allele that confers increased low-oxygen fitness ($hrmA^{R\text{-}EV}$) (30) generates a more robust 24-h biofilm compared to the control strain AF293 (Fig. 2*D*). These mutant strains support the observation that hypoxic microenvironments develop during filamentous fungal biofilm maturation and that hyphal growth in the context of these oxygen gradients drives the emergence of mature fungal biofilm architecture including vertically aligned branching networks.

A Hypoxic Response Is Spatially Induced in Filamentous Fungal Biofilms and Associated with Reduced Translational Activity in Individual Hyphae. Our results indicate that *A. fumigatus* biofilm architecture is highly dependent on prevailing oxygen concentrations, and that as these biofilms mature they deplete the local oxygen supply in the basal layers of their own structure. Consequently, these data suggest that basal areas of the biofilm may induce a physiological hypoxia response to the changing microenvironment they occupy. To examine the spatial distribution of a hypoxia response in a filamentous fungal biofilm, we generated a hypoxia response transcriptional reporter with green fluorescent protein (GFP) and counterstained all biomass with the cell-wall-binding compound calcofluor white. The hypoxia reporter was generated using the *erg25A* promoter, an ergosterol biosynthetic gene encoding a C4-sterol methyloxidase that has low transcript counts at ~21% oxygen and high transcript counts at 0.2% oxygen (*SI Appendix*, Fig. S5*A*) (30). Introduction of the reporter did not impact growth of *A. fumigatus* (*SI Appendix*, Fig. S5*B*), and GFP signal could be differentiated from background signal by 40 min of exposure to 0.2% oxygen in swollen conidia (*SI Appendix*, Fig. S5*C*). Twelve-hour biofilms of the hypoxia reporter strain ($_{p}erg25A$-GFP) have no detectable signal in normal oxygen, but when shifted to 0.2% oxygen for 1 h all hyphae fluoresce (Fig. 3 *A* and *B* and *SI Appendix*, Fig. S6*A*). Modeling predicts that hypoxic zones occur between 14 h and 16 h (Fig. 2*C*), and we observe GFP fluorescence concentrated at the base of 16-h, 18-h, and 24-h biofilms (Fig. 3 *A* and *B* and *SI Appendix*, Fig. S5*A*). Mature 16-h biofilms cultured on oxygen-permeable plates are devoid of signal, indicating the absence of a detectable hypoxic zone under these conditions (Fig. 3 *C* and *D* and *SI Appendix*, Fig. S6*B*).

Anoxic regions are also predicted to occur as the biofilm develops, which may contribute to the reduction in hypoxia reporter signal at 18 h and 24 h relative to 16 h (44). To further examine this observation, a translational activity reporter strain was constructed. GFP translation and resulting fluorescence following exogenous induction of the reporter serves as a marker for translationally active cells. Cells in a quiescent or translationally inactive state will not express GFP, or will more slowly express it, following transcriptional induction (37). We constructed a xylose-inducible GFP reporter system (45), as the small size of this monosaccharide allows for simple diffusion through hyphae within the biofilm (where space between hyphae ranges from 20 to 30 μm). The induced GFP signal is specific for addition of xylose and observed above background after 45 min of induction (*SI Appendix*, Fig. S7*A*). Xylose induction in a mature biofilm with the translational reporter system $_{p}xylP$-GFP

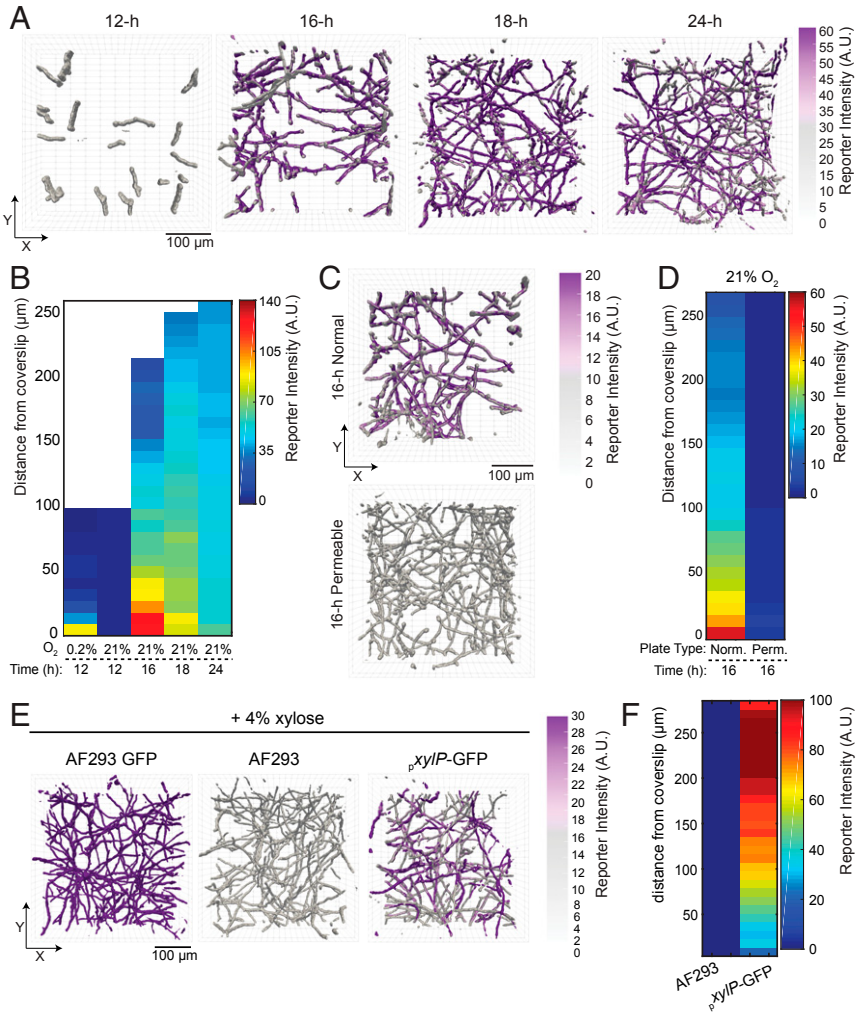

Fig. 3. The spatial and temporal hypoxic zone coincides with a reduced metabolic state. (*A*) Single representative 3D rendered micrographs of $n = 3$ independent biological samples show visible $_p$*erg25A*-GFP reporter signal at 16-h, 18-h, and 24-h biofilms but absent at 12 h. (Scale bar, 100 µm.) (*B*) Heat map of the hypoxia-reporter signal relative to fungal biomass. Each column is representative of $n = 3$ independent biological samples. (*C*) Single representative 3D rendered micrographs of $n = 3$ independent biological samples show an absence of $_p$*erg25A*-GFP reporter signal in 16-h biofilms cultured on oxygen-permeable surfaces. (Scale bar, 100 µm.) (*D*) Heat map of the hypoxia-reporter signal relative to fungal biomass for 16-h biofilms grown on normal or oxygen permeable surfaces. Each column is representative of $n = 3$ independent biological samples. (*E*) Xylose-inducible GFP expression indicates translational activity within the vertically grown hyphae of 18-h biofilms after 3 h of induction but absent from the horizontal hyphae at the base. Images are representative 3D renderings from $n = 3$ independent biological samples. (Scale bar, 100 µm.) (*F*) Heat map quantifying GFP fluorescence relative to overall biomass from images in *A*. Each column is representative of a single sample from $n = 3$ biological samples.

(18 h plus 3-h xylose induction) results in GFP signal localized to the vertically aligned hyphae within the predicted normoxic zone. In the hypoxic zone at the base, signal was largely, but not completely, absent (Fig. 3 *E* and *F* and *SI Appendix*, Fig. S7*B*). The signal is specific for induction with xylose (*SI Appendix*, Fig. S7*B*) and absent in an isogenic parent strain lacking the reporter (Fig. 3 *E* and *F*). Importantly, for a strain containing a constitutive GFP-expressing construct (AF293^{GFP}), GFP signal is visible at all depths of the biofilm, indicating the presence of enough oxygen throughout the biofilm for GFP folding and fluorescence (Fig. 3 *E* and *F* and *SI Appendix*, Fig. S7*B*). These data indicate that reduced translational activity occurs within the basal hypoxic microenvironments in mature filamentous fungal biofilms.

Fungal-Induced Hypoxic Microenvironments Facilitate Biofilm Antifungal Drug Resistance. Because current antifungal agents target metabolically active fungal cells, we hypothesized that self-induced hypoxic microenvironments facilitate antifungal drug resistance. As an important note, we use the term "resistance" herein to describe the biofilm phenotype of persistent fungal metabolic activity and reduced drug susceptibility in the face of antifungal drug treatment. We alternatively considered the use of "tolerance" that has been more rigorously defined in the context of planktonic yeast cell populations, but it remains unclear if the reduced drug susceptibility of hypoxic hyphae within the biofilm meet the accepted tolerance definition for planktonic cells (9, 46).

To test the hypothesis that fungal-induced hypoxic microenvironments facilitate antifungal drug resistance, we first treated biofilms with the contemporary drugs voriconazole and amphotericin B at different stages of growth that correspond with different levels of oxygen depletion. Twelve-hour biofilms are significantly more sensitive to antifungal treatment and oxidative stress (menadione) compared to 16-h and 20-h biofilms, as measured using the tetrazolium dye XTT (where percent damage corresponds to the reduction in metabolic activity of the biofilm) (Fig. 4*A*). Drug sequestration by ECM is the current known mechanism of fungal biofilm drug resistance in *Candida*

albicans (19), Therefore, we examined the drug resistance of mature 18-h *A. fumigatus* biofilms deficient in the major ECM component exopolysaccharide galactosaminogalactan. A null mutant of the UDP-glucose 4-epimerase (Δ*uge3*) critical for ECM formation surprisingly remains resistant to antifungals (Fig. 4*B*). Therefore, other filamentous fungal biofilm-dependent phenotypes contribute to the antifungal recalcitrance of these surface-adhered populations. We next turned our attention to the hypoxic microenvironments generated during biofilm maturation.

To determine if a reduction in environmental oxygen availability is sufficient to generate antifungal drug resistance as it affects biofilm architecture, we grew 12-h and 18-h biofilms at ambient oxygen (21% O_2) or at 0.2% O_2 and then treated with voriconazole, amphotericin B, or menadione. The 12-h biofilms show significantly reduced damage when treated at 0.2% O_2 for all three agents (Fig. 4*C*). This trend was observed using two independent methods for cell viability (*SI Appendix*, Fig. S8) and across three additional strains of *A. fumigatus* (*SI Appendix*, Fig. S9). Eighteen-hour biofilms, which have zones of naturally depleted oxygen and intrinsically exhibit drug resistance, show no significant changes in antifungal-induced damage when treated at 0.2% O_2 versus at 21% O_2 (Fig. 4*C*). However, 18-h biofilms cultured and treated on oxygen-permeable surfaces, where oxygen is significantly increased (Fig. 4*D*), are significantly more sensitive to all three agents (Fig. 4*E*). Additionally, when grown on oxygen permeable plates mature biofilms of the polymorphic yeast *C. albicans* also have significantly increased oxygen compared to growth on normal plates (*SI Appendix*, Fig. S10). Accordingly, *C. albicans* biofilms grown on these oxygen-permeable plates are also significantly more sensitive to amphotericin B (*SI Appendix*, Fig. S10).

Hypoxic zones at the biofilm base are predicted through modeling to result from oxygen consumption by biomass closer to the air–liquid interface, as opposed to physical obstacles to oxygen diffusion. To test whether fungal oxygen consumption self-induces hypoxia that protects specific hyphae from antifungal drug treatment, we cultured biofilms in conditions predicted to increase oxygen consumption: incubation with the mitochondrial uncoupler FCCP [carbonyl cyanide 4-(trifluoromethoxy) phenylhydrazone] and growth in media supplemented with tricarboxylic acid cycle (TCA) intermediates. FCCP was previously shown to increase *A. fumigatus* oxygen consumption rates (41), and FCCP treatment of 24-h biofilms significantly reduces dissolved oxygen at 2.5 mm below the air–liquid interface compared to controls after only 30 min of exposure (Fig. 5*A*). Cotreatment of 12-h biofilms with FCCP significantly reduces the metabolic activity inhibition (percent damage) caused by amphotericin B treatment (Fig. 5*B*). Shifting 24-h biofilms to media with TCA intermediates (respiratory minimal media) results in significantly reduced dissolved oxygen at 2.5 mm below the air–liquid interface compared to media with 1% glucose (Fig. 5*C*). Treatment of 12-h biofilms with amphotericin B in respiratory minimal media remarkably results in significantly less damage, as measured by an increase in metabolic activity, than treatment in minimal media with glucose (Fig. 5*D*). Together these data support a model where hypoxic microenvironments occur due to fungal oxygen consumption within mature biofilms, and once established they facilitate resistance to antifungal treatment.

Cells within the Hypoxic Microenvironment Endure Treatment and Reinitiate Growth. Our data suggest that hyphal oxygen consumption in the biofilm contributes to the phenotype of biofilm antifungal drug resistance. Therefore, we hypothesized that antifungal treatment would reduce oxygen consumption and increase dissolved oxygen within the biofilm. After 1.5 h of treatment with either voriconazole (fungistatic) or amphotericin B (fungicidal), we observed an increase in dissolved oxygen for

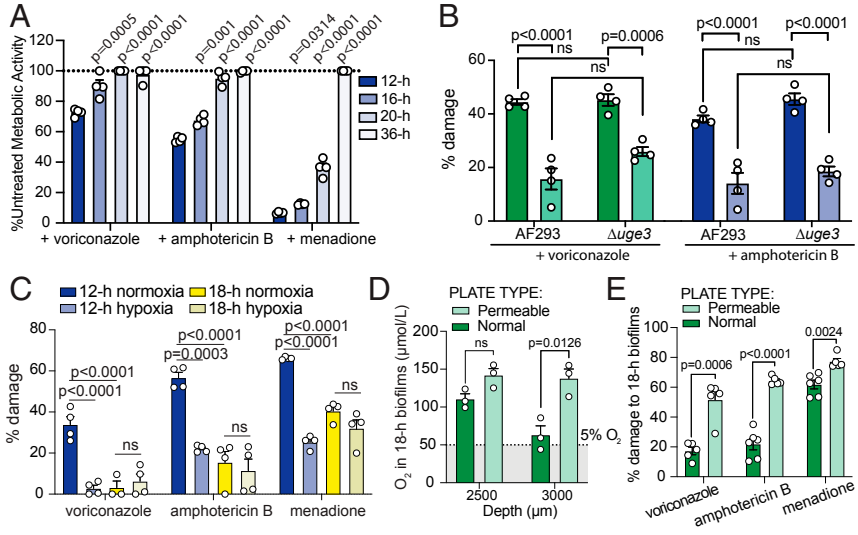

Fig. 4. Hypoxia contributes to biofilm antifungal drug resistance. (*A*) Biofilms become increasingly resistant to exogenous stressors (voriconazole: 1 μg/mL, amphotericin B: 1 μg/mL, menadione: 10 μM) throughout maturation. Error bars indicate SEM with $n = 3$ independent biological samples. (*B*) Eighteen-hour biofilms remain largely resistant to treatment with voriconazole (1 μg/mL) or amphotericin B (1 μg/mL) with (AF293) or without (Δ*uge3*) the production of the exopolysaccharide galactosaminogalactan. Error bars indicate SEM for $n = 4$ biologically independent samples. One-way ANOVAs performed with Tukey's multiple comparison test. (ns: $P > 0.05$, not significant). (*C*) Twelve-hour biofilms are significantly more susceptible to antifungals (voriconazole: 1 μg/mL, amphotericin B: 1 μg/mL, menadione: 10 μM) than 18-h biofilms in normoxia (21% O_2). Treatment in hypoxia (0.2% O_2) significantly reduces the susceptibility of 12-h biofilms but not 18-h biofilms. Error bars indicate SEM of $n = 4$ independent biological samples. Each treatment group was analyzed separately with a one-way ANOVA with Tukey's multiple comparison test. (*D*) Eighteen-hour biofilms on oxygen-permeable plates have significantly more oxygen at a depth of 3 mm. Error bars indicate SEM of $n = 3$ independent biological samples. Student's *t* test performed between samples at each depth. (*E*) Eighteen-hour biofilms are significantly more susceptible to treatment on oxygen-permeable surfaces. Error bars indicate SEM of $n = 5$ or $n = 6$ independent biological samples. Student's unpaired two-tailed *t* test performed between samples within each treatment group.

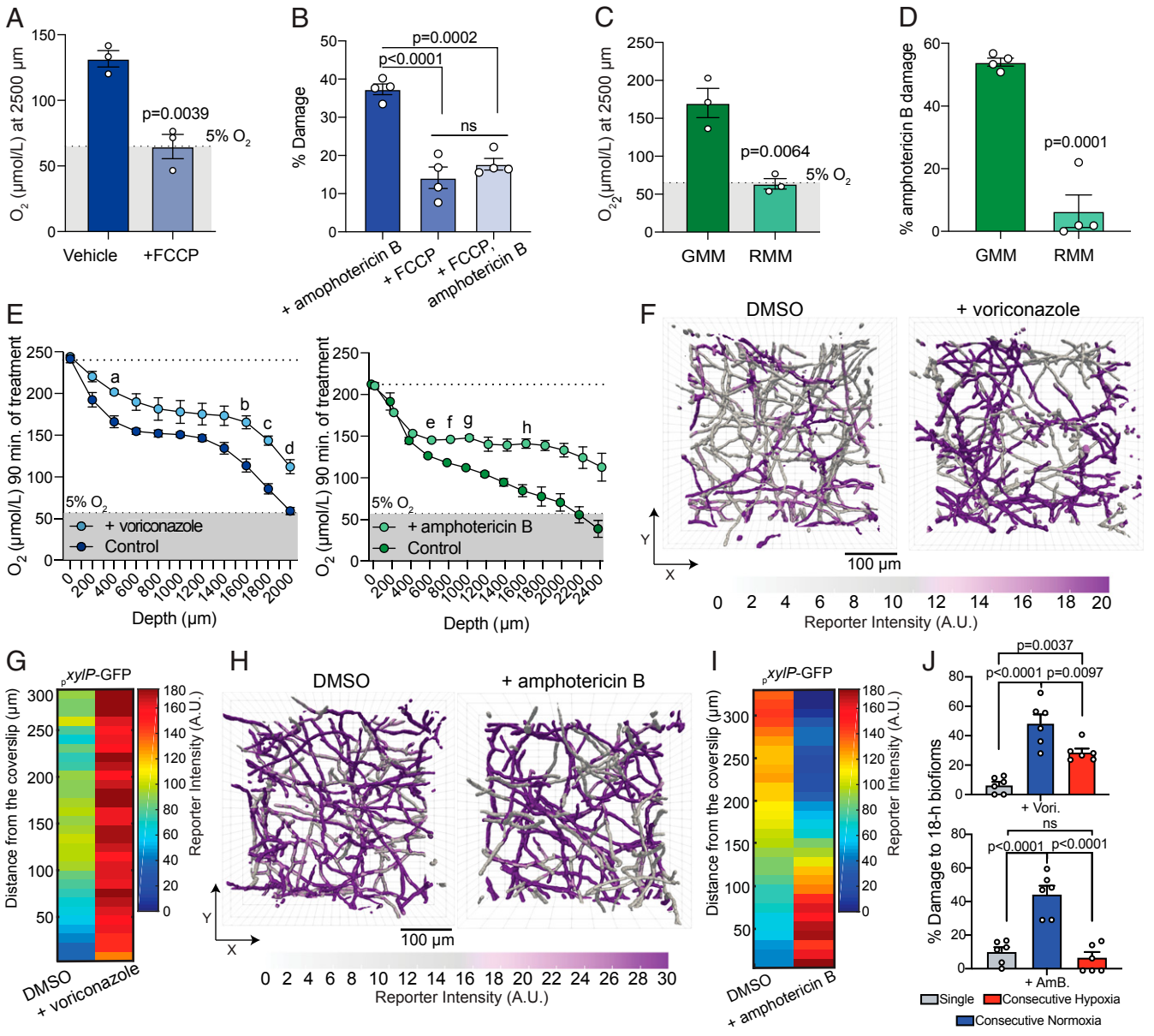

Fig. 5. Respiration-induced hypoxic zones reoxygenate after treatment to facilitate biofilm growth and drug resistance. (*A*) FCCP (2.5 μM) significantly reduces dissolved oxygen in 24-h biofilms after 30 min. Error bars indicate SEM of $n = 3$ independent biological samples. Student's unpaired two-tailed *t* test performed. (*B*) FCCP significantly reduces amphotericin B damage in 12-h biofilms. Error bars indicate SEM of $n = 4$ independent biological samples. One-way ANOVA with Sidak's multiple comparison test performed. (*C*) Incubation in RMM that contains TCA intermediates significantly reduces dissolved oxygen in 24-h biofilms compared to incubation in GMM. Error bars indicate SEM of $n = 3$ independent biological samples. Student's unpaired two-tailed *t* test performed. (*D*) Treatment of 12-h biofilms in RMM significantly reduces amphotericin B damage compared to treatment in GMM. Error bars indicate SEM of $n = 4$ independent biological samples. Student's unpaired two-tailed *t* test performed. (ns = $P > 0.05$, not significant). (*E*) Antifungal treatment with voriconazole (1 μg/mL) or amphotericin B (1 μg/mL) significantly increases dissolved oxygen within the 24-h biofilms after 90 min of treatment. Error bars indicate SEM of $n = 4$ independent biological samples. Comparisons were made using a multiple *t* test approach with the Holm–Sidak method to determine statistical significance: (a) $P = 0.003190$, (b) $P = 0.003288$, (c) $P = 0.000443$, (d) $P = 0.001435$, (e) $P = 0.003119$, (f) $P = 0.000011$, (g) $P = 0.000312$, (h) $P = 0.003331$. Comparisons without a *P* value listed are $P > 0.05$ and not statistically significant. (*F*) Voriconazole (1 μg/mL) treatment increases the xylose-inducible signal for translation activity at the base of the biofilm. Images representative of $n = 3$ independent biological samples. (Scale bar, 100 μm.) (*G*) Heat map quantifying GFP fluorescence relative to overall biomass from images in *F* shows visible signal at the base of the 18-h biofilm following voriconazole treatment. Each column is representative of $n = 3$ independent biological samples. (*H*) Amphotericin B (1 μg/mL) treatment largely reduces the xylose-inducible signal for translation activity. Visible signal is localized only at the base of the 18-h biofilm. Images representative of $n = 3$ independent biological samples. (Scale bar, 100 μm.) Each column is representative of $n = 3$ independent biological samples. (*I*) Heat map quantifying GFP fluorescence relative to overall biomass from images in *H* shows visible signal at the base of the 18-h biofilm following amphotericin B treatment. Each column is representative of $n = 3$ independent biological samples. (*J*) Consecutive treatments with voriconazole. or amphotericin B in normoxia significantly increases the damage to 18-h AF293 biofilms, while consecutive treatments in hypoxia cause significantly less damage than in normoxia. Error bars indicate SEM of $n = 6$ independent biological samples. One-way ANOVA with Tukey's multiple comparisons test performed. (ns: $P > 0.05$, not significant).

both treatment groups (Fig. 5*E*). Two hours after drug removal, only those biofilms that received amphotericin B treatment had significantly increased dissolved oxygen (*SI Appendix*, Fig. S11 *A* and *B*). To determine if increased dissolved oxygen during treatment allows for the hyphae at the base of the biofilm to become more translationally active, we utilized the $_{p}$*xylP*-GFP

metabolic reporter in the presence and absence of voriconazole and amphotericin B. Following 3-h voriconazole treatment of 18-h biofilms we induced GFP with xylose and observed an increase in the translational activity at the base of the biofilm (Fig. 5 *F* and *G* and *SI Appendix*, Fig. S11*C*). Similarly, treatment with amphotericin B dramatically reduces fluorescence within vertically aligned hyphae, and the only visible signal for active GFP translation is concentrated at the base of the biofilm (Fig. 5 *H* and *I* and *SI Appendix*, Fig. S11*D*). Importantly, mature untreated or vehicle-treated biofilms grown on oxygen-permeable surfaces have homogenous signal for active GFP translation indicating homogenous increased rates of translation (*SI Appendix*, Fig. S12). Treatment of these biofilms with the fungistatic agent voriconazole mildly increases translation reporter signal after 3 h of recovery, while treatment with the fungicidal agent amphotericin B largely reduces overall signal from the translational reporter (*SI Appendix*, Fig. S12).

To investigate if increased translational activity within the biofilm sensitizes the biofilm to antifungal treatment, we performed consecutive dosing of antifungal drugs with 18-h biofilms. Consecutive doses of voriconazole or amphotericin B at ambient oxygen (normoxia, 21% O_2) significantly increases the damage to the biofilms (reduces metabolic activity) compared to the single-dose control (Fig. 5*J*). In contrast, a consecutive dose at 0.2% O_2 (hypoxia) results in a significantly smaller reduction in metabolic activity than in normoxia (Fig. 5*J*). This was true for two independent *A. fumigatus* strains (*SI Appendix*, Fig. S13). Taken together, our results highlight that self-induced hypoxic microenvironments arise as a result of fungal oxygen consumption in the maturation of *A. fumigatus* biofilms. The hypoxia response of fungal cells that manifests as a result of these self-generated hypoxic zones leads to reduced metabolic activity in the basal biofilm layers; the cells in these basal layers then serve as a drug-resistant reservoir of viable biomass that reseeds the fungal biofilm once drug treatment diminishes or is ceased (*SI Appendix*, Fig. S14).

Discussion

Filamentous fungal biofilms present with unique morphology and architecture that is distinct from bacterial and yeast biofilms (29). How these unique filamentous fungal morphologies impact fungal disease relevant outcomes remains unclear. Here we observe that *A. fumigatus* biofilms consistently develop spatial gradients of hypoxic microenvironments during their maturation. The formation of these hypoxic zones contributes not only to the emergent architecture of the growing biofilm but also functionally in the form of antifungal drug resistance. The spatially defined hypoxic microenvironments in *A. fumigatus* biofilms occur as a natural consequence of the metabolic activity of the growing hyphal network away from the surface and toward the oxygen supply. These hypoxic regions coincide with spatially distinct hyphae at the biofilm base that are in what is likely a reduced or quiescent metabolic state. The spatial constriction of these quiescent hyphae to the hypoxic zone suggests that they arise as the result of the growing filamentous network geometry in relation to their basal anchoring surface and location of the oxygen source. Thus, the fundamental mechanism of hypoxic region generation begins with what appears to be aerotropic hyphal growth away from an origin point and toward an oxygen source. This concerted growth toward the oxygen source leads to oxygen depletion within the inner layers of the growing network. In our experiments, the oxygen source was the air–liquid interface of culture dishes, but this principle applies to any arbitrary environment in which hyphal networks begin to grow away from a seeding spore and toward a source of oxygen elsewhere (47).

Despite the well-established occurrence of oxygen depletion in densely occupied bacterial and yeast biofilms, this observation in a filamentous fungal biofilm is surprising to us given the unique open architecture of hyphal cell arrangements. How *A. fumigatus* and other filamentous fungi are able to sense changes in oxygen and potentially polarize growth along oxygen gradients remains an intriguing question and is the focus of ongoing research. Notably, in *A. nidulans*, the hypoxia response transcription factor SrbA has been implicated in microtubule depolarization within mature biofilms in response to altered gaseous environments (48). These data may suggest that the directionality of hyphal growth toward the air–surface liquid interface is driven in part by SrbA-mediated regulation of microtubule depolarization, and this remains to be tested in *A. fumigatus*.

An outstanding question from the results presented here concerns the mechanism(s) of hypoxic microenvironment-mediated drug resistance within biofilms. Despite the fact that low-oxygen regions appear common in bacterial and fungal biofilms, mechanistic studies linking the hypoxic response within biofilms and antimicrobial resistance are largely absent among eukaryotic human pathogens (35, 37, 39, 49). To date, biofilm antifungal drug resistance has been best-studied with the polymorphic yeast *C. albicans*, and while low-oxygen environments have been detected within these fungal biofilms, a mechanistic link between low oxygen and antifungal resistance has not been explicitly shown. Instead a number of other aspects of *C. albicans* biofilm growth have been linked to antifungal resistance, including β-glucan in the ECM (19), expression of efflux pumps (23, 25, 50), metabolic changes (23, 51), cell-wall stress responses (52), and the occurrence of putative yeast persister cells (however, the existence of yeast persister cells remains controversial) (13, 53). Our observation here that amphotericin B sensitivity of *C. albicans* biofilms is significantly increased on oxygen-permeable plates poses the intriguing question of how the hypoxic microenvironments within a biofilm may impact these other characterized aspects of fungal physiology linked to antifungal resistance (i.e., efflux pump expression, matrix modulation, cell wall, etc.). Further work, coupled with existing detailed studies of *C. albicans* biofilm development (51, 54, 55), is required to determine how hypoxic microenvironments in yeast biofilms contribute to drug resistance.

Concerning *A. fumigatus*, previous studies have not detected increases in resistance to amphotericin B, various azoles, or the echinocandin caspofungin in low-oxygen compared to normal-oxygen conditions (56, 57). These studies, however, were performed with planktonic hyphal cells and were designed such that oxygen limitation was uniform throughout the culture and at the start of growth by the planktonic hyphal cells of *A. fumigatus*. Thus, growth of filamentous fungal cells in a low-oxygen environment is not by itself sufficient to drive antifungal drug resistance. This of course raises intriguing questions about the physiological state and phenotypes of the drug-resistant hyphae experiencing hypoxic stress in the biofilm environment. For example, the presence of environmental DNA (20) within biofilms and elevated efflux pump activity (24) has been suggested to contribute to *A. fumigatus* biofilm drug resistance. It remains unclear if the hypoxic regions within *A. fumigatus* biofilms increases the spatially restricted expression or activity of efflux pumps that contribute to antifungal resistance, as has been observed with *Pseudomonas aeruginosa* (37). A recent study has implicated efflux pump activity in *A. fumigatus* antifungal resistance as a result of mitochondrial dysfunction and aberrant calcium signaling, but this has not yet been investigated in the context of fungal biofilms as a potential mechanism of drug resistance (58). It remains an interesting and important question if altered mitochondria function, as a direct result of low-oxygen stress (41), impacts calcium signaling to contribute to *A. fumigatus* hypoxia-induced drug resistance in biofilms.

Importantly, we demonstrate in vitro that replenishing oxygen to the fungal biofilms through growth on oxygen-permeable plates or through consecutive antifungal treatment strongly reduces or eliminates the biofilms' drug resistance. One approach to mitigate this problem in a clinical setting could be to increase

oxygen tension to damaged tissue; hyperbaric oxygen treatment has typically been used in the clinic to achieve this goal. Hyperbaric oxygen treatment has fungal biofilm growth-arresting capabilities in vitro, but this treatment surprisingly failed to synergize with the antifungals voriconazole or amphotericin B in vitro and in vivo (59). The reduced growth rate in response to oxygen supplementation perhaps counterintuitively drives a biofilm hypoxia-related phenotype, preventing increased efficacy of the antifungals. Future work investigating how *A. fumigatus* senses oxygen will be important in understanding the mechanisms of oxygen-mediated antifungal drug resistance and critical to identify potential targets and/or approaches to sensitize the entire fungal biofilm to antifungal drugs regardless of the oxygen environment and fungal metabolic state. One seminal example of this concept is the observation that *P. aeruginosa* aggregate biofilms display oxygen-dependent differential sensitivity to tobramycin and chlorate, with chlorate selectively targeting anaerobic cells (60). Thus, the extension of oxygen gradient-mediated microbial biofilm drug resistance to the fungal kingdom paves the way for future new therapeutic approaches that are expected to impact both bacterial and fungal biofilms in vivo.

Materials and Methods

Strains and Growth Culture Conditions. All strains utilized in this study are listed in *SI Appendix*, Table S1. Strains were cultured on 1% glucose minimal media [GMM; 1% glucose, 6 g/L $NaNO_3$, 0.52 g/L KCl, 0.52 g/L $MgSO_4•7H_2O$, 1.52 g/L KH_2PO_4 monobasic, 2.2 mg/L $ZnSO_4•7H_2O$, 1.1 mg/L H_3BO_3, 0.5 mg/L $MnCl_2•4H_2O$, 0.5 mg/L $FeSO_4•7H_2O$, 0.16 mg/L $CoCl_2•5H_2O$, 0.16 mg/L $CuSO_4•5H_2O$, 0.11 mg/L $(NH_4)_6Mo_7O_{24}•4H_2O$, and 5 mg/L Na_4EDTA; pH 6.5]. For solid media agar was added to 1.5%. Conidia were collected for experiments after growth at 37 °C and 5% CO_2 for 72 to 96 h by flooding the plate with 0.01% Tween-80 and filtering through Miracloth (Millipore Sigma). Respiratory minimal media [RMM; 6 g/L $NaNO_3$, 0.52 g/L KCl, 0.52 g/L $MgSO_4•7H_2O$, 1.52 g/L KH_2PO_4 monobasic, 2.2 mg/L $ZnSO_4•7H_2O$, 1.1 mg/L H_3BO_3, 0.5 mg/L $MnCl_2•4H_2O$, 0.5 mg/L $FeSO_4•7H_2O$, 0.16 mg/L $CoCl_2•5H_2O$, 0.16 mg/L $CuSO_4•5H_2O$, 0.11 mg/L $(NH_4)_6Mo_7O_{24}•4H_2O$, 5 mg/L Na_4EDTA, 10 mM glutamate, 10 mM malate, 10 mM pyruvate, and 10 mM α-ketoglutarate; pH 6.5] was filter-sterilized. For agar plate growth assays 10^3 conidia are inoculated in 2 μL 0.01% Tween-80 at the center of the plate and incubated for 96 h at 37 °C, 5% CO_2 in ambient air (21% O_2) or at 0.2% O_2. The low-oxygen conditions (0.2% O_2, 2% O_2, 5% O_2, and 10% O_2) were maintained using an INVOVO2 400 hypoxia chamber (The Baker Company).

Strain Construction. The reference strain AF293 was used to generate the reporter strains $_p$*erg25A-gfp* and $_p$*xylP-gfp*. The *erg25A* promoter was selected as the 672 base pairs (bp) immediately upstream of the *erg25A* (Afu8g02440) start codon in AF293 identified using FungiDB.org (61). The *Penicillium chrysogenum* xylanase (*xylP*) promoter was ordered as a gBlock from Integrated DNA Technologies based on the published sequence (GenBank accession no. M98458.2) (45). Both reporter constructs are designed with *mGFP5* and the *trpC* terminator from *Aspergillus nidulans* and the dominant marker for pyrithiamine resistance, *ptrA* (62). For the overexpression of *mGFP5* in Δ*srbA* and *hrmA*$^{R\text{-}EV}$, mGFP5 is expressed by the strong *A. nidulans* glyceraldehyde-3-phosphate dehydrogenase (*gpdA*) promoter with the *trpC* terminator and *ptrA* or *hygB*, for Hygromycin B resistance (63). All constructs were integrated ectopically into the chromosomes using protoplasting and transformation protocols as previously described (43, 47).

Fluorescence Microscopy of Fungal Biofilms.

Microscopy equipment. Fluorescence confocal microscopy was performed on either an Andor W1 Spinning-Disk confocal with a Nikon Exlipse Ti inverted microscope equipped with Perfect Focus with a CFI Plan Apochromat 10XC Glyc objective (Nikon) or CFI Plan Fluor 20XC MI (Nikon) or a Zeiss LSM880 with a C-Apochromat 10×/0.45 W M27 objective (Zeiss).

Biofilm sample preparation. *A. fumigatus* biofilms were cultured for imaging in MatTek dishes ("normal plates," P35G-1.0-14-C; MatTek) or in gas-permeable slide plates ("permeable plates," 8602003; Coy Lab Products), with or without a gas-impermeable seal, in GMM broth inoculated with 10^5 conidia per mL with 2 mL per dish. *A. nidulans* and *S. apiospermum* biofilms were imaged similarly but in Czapek-dox media (Difco). For *A. fumigatus* biofilms at 21% O_2, the incubation time was 24 h unless otherwise noted. For *A. fumigatus* biofilms at 0.2%, 2%, 5%, or 10% O_2 the incubation time was 48 h unless otherwise noted. *S. apiospermum* biofilms in 21% and 0.2% O_2 were incubated for 48 h. *A. nidulans* biofilms in 21% and 0.2% O_2 were incubated for 24 h and 48 h, respectively. All biofilms were grown at 37 °C with 5% CO_2.

For the $_p$*erg25A-gfp* biofilms incubation times are as listed. For the 12-h biofilm at 0.2% O_2, the biofilm was incubated at 21% O_2 for 12 h and then shifted for 1 h to 0.2% O_2 before imaging. For the $_p$*xylP-GFP* biofilms incubation times are as listed. Following incubation, biofilms were washed once with phosphate-buffered saline (PBS) and incubated for 3 h with 4% xylose (in minimal media minus glucose) for the induction of the reporter.

Biofilm imaging. For strains not constitutively expressing GFP, the fungi were stained with calcofluor white (CFW) (Fluorescent Brightener 28, F3543; Sigma) at a final concentration of 25 μg/mL water for 15 min. GFP and CFW biofilms were imaged at 488 nm and 405 nm, respectively. Images captured with the CFI Plan Apochromat 10XC Glyc objective (Nikon) are at heights of 500 to 1,800 μm, images captured with the C-Apochromat 10×/0.45 W M27 objective (Zeiss) are at heights of 500 to 900 μm, and images captured with the CFI Plan Fluor 20XC MI (Nikon) are at heights of ∼300 μm. XZ images of biofilms in *SI Appendix*, Figs. S6 and S9 are were processed in the Nikon Elements Viewer for 3D rendering and processing a depth of 200 μm or 500 μm.

Quantification of Biofilm Density, Architecture, and Reporter Signals. All image data were analyzed using the BiofilmQ framework written in MATLAB (64). The framework is freely available for download at https://drescherlab.org/data/biofilmQ/. Biofilm visualizations were generated using the.vtk file output capability within BiofilmQ and rendered using Paraview, also freely available at https://www.paraview.org/.

Drug Treatment Assays.

Biofilm sample preparation. Biofilms were cultured in 24-well Falcon polystyrene microplates (08-772-1H; Fisher) (normal plates) or 24-well gas-permeable plates (8602000; Coy Lab Products) (permeable plates) with 10^5 conidia per mL of GMM broth (0.5 mL per well) at 37 °C, 5% O_2, and 21% O_2 for the times listed. For the nonadherent strain Δ*uge3* and the AF293 controls, the 24-well Falcon polystyrene microplate was coated for 12 h with collagen coating solution (125-50; Sigma) at room temperature to facilitate adherence.

For *C. albicans* biofilms strain SC5314 was utilized. SC5314 was cultured in yeast extract–peptone–dextrose overnight at 30 °C on a rotating culture wheel and then subcultured for 6 h in the same conditions. Cells were washed three times with 1× PBS and diluted to 10^6 cells per mL in RPMI 1640 (+ L-glutamine, − phenol red). Biofilms were seeded with 0.5 mL per well of a normal polystyrene 24-well culture plate or an oxygen-permeable 24-well culture plate (Coy Labs) and incubated at 37 °C with 5% CO_2 for 18 or 36 h.

Drug treatments. Following incubation, biofilms were washed once with 0.5 mL sterile 1× PBS. Biofilms were treated for 3 h with the vehicle controls (dimethyl sulfoxide [DMSO] or ethanol), voriconazole (1 μg/mL DMSO) (PZ0005; Sigma), amphotericin B (1 μg/mL DMSO) (11636; Cayman Chemicals), or menadione/vitamin K3 (10 μM in 95% ethanol) (50-793-4; Fisher). Drug treatment was performed in GMM unless otherwise noted. Cotreatment with FCCP (mesoxalonitrile 4-trifluoromethoxyphenylhydrazone) (C2920; Sigma) was performed at 2.5 μM in DMSO.

For consecutive drug treatments, the initial treatment was performed as described above in 21% O_2. Following this 3-h initial treatment, biofilms were washed once with PBS and a second identical dose of antifungal was applied to the biofilm in 21% O_2 or 0.2% O_2. This was performed for two independent strains of *A. fumigatus*.

For *C. albicans* biofilms, biofilms were washed once with 0.5 mL sterile 1× PBS. Biofilms were treated for 6 h with DMSO (vehicle control), 1 μg/mL amphotericin B, 0.6 μg/mL amphotericin B, or 0.3 μg/mL amphotericin B (11636; Cayman Chemicals). Treatment was performed at 37 °C with 5% CO_2 at ambient oxygen.

XTT assay. After 3 h of treatment, the drug or vehicle was removed and the biofilms were washed once with 0.5 mL 1× PBS. XTT [2,3-bis-(2-methoxy-4-nitro-5-sulfophenyl)-2H-tetrazolium-5-carboxanilide] solution (0.5 mg XTT/mL 1× PBS with 25 μM menadione) (XTT sodium salt, ab146310; Abcam) was added at 0.3 mL per well and incubated at 37 °C, 5% CO_2, and 21% O_2 until the positive vehicle control wells were reduced (1 to 3 h). The XTT solution supernatant was transferred to a 96-well Falcon Polystyrene microplate (08-772-5; Fisher) and optical density was measured at 490 nm. Drug-treated wells were compared to vehicle-treated wells to calculate the reduction in metabolic activity (or damage) to the biofilm as a result of antifungal treatment.

Resazurin assay. After 3 h of treatment, the drug or vehicle was removed and the biofilms were washed as described for the XTT assay above. A 10% resazurin (TOX8; Sigma) solution was prepared in 1× PBS and added to the biofilms at 0.3 mL per well. The biofilms were incubated at 37 °C, 5% CO_2, and 21% O_2 until the control untreated wells turned from blue (unreduced) to red (reduced) (2 to 4 h). The resazurin supernatant was analyzed spectrophotometrically at 690 nm (reference optical density) and 600 nm (unreduced resazurin dye). Percent damage, a metric of change in metabolic activity, was calculated by comparing the drug-treated wells to the vehicle-treated controls and resazurin-only wells.

Dissolved Oxygen Quantification.

Unisense equipment and software. Dissolved oxygen was quantified using a Unisense Oxygen Measuring System 1-CH (Unisense OXY METER) equipped with a micromanipulator (Unisense MM33), motorized micromanipulator stage (Unisense MMS), motor controller (Unisense MC-232), and a 25-μm Clark-type/amperometric oxygen sensor (Unisense OX-25). The readers were automated and analyzed through SensorTrace Suite Software v3.1.151 (Unisense STSUITE).

Biofilm sample preparation. Biofilms were prepared at 10^5 conidia per mL in 4 mL GMM broth unless otherwise noted and incubated at 37 °C, 5% CO_2, and 21% O_2 for the described time. As noted, biofilms were prepared in Falcon 35-mm polystyrene Petri dishes (normal plates, 351008; Fisher) or gas-permeable slide plates (permeable plates, 8602003; Coy Lab Products).

C. albicans biofilms were prepared as described above for the drug treatment assays.

Oxygen quantification. The microelectrode was manually position at the air–liquid interface of the biofilm with the micromanipulator (Unisense MM33). This starting position is ∼3 mm above the fungal growth at 24 h and is considered a depth of 0 μm. The motorized stage was set to record oxygen measurements in technical duplicates at 200-μm or 500-μm intervals from this starting position. At each position the microelectrode waited 10 s to equilibrate before measuring for an additional 10 s and recording the average. Three separate XY positions in the biofilm were measured in technical duplicates at each depth. This was repeated for a minimum of three biological replicates per condition. Samples where the biomass had become detached or visually disrupted were omitted. Due to the fragility of the microelectrodes depths greater than 2.5 to 3 mm were not attempted.

Modeling of Fungal Biofilm Maturation.

Estimation of biomass density. Here we estimate the distribution of biomass density along the biofilm's height over time, based on microscopy data from the bottom 570 μm of the biofilm at different time points during development and from the full mature biofilm at 24 h. For each imaged horizontal layer of the biofilm (biofilm height), we use a sigmoidal curve $d(t) = d_f/[1 + \exp(-m(t - t_h))]$ to fit the biomass density growing in time until it reaches the mature biofilm density, with parameters t_h indicating the time at which that height is reached, m indicating the speed at which the biofilm matures at that height, and d_f indicating the final biomass density (*SI Appendix*, Fig. S3*A*). We used imaging layers where intermediate biomass densities were sampled by at least two time points to determine the variations of parameters m and t_h with biofilm height, further approximating this variation with a linear fit in order to estimate the biofilm density at heights that could not be imaged during the experiment (*SI Appendix*, Fig. S3 *B* and *C*). The final biomass density was determined using imaging data from the full mature biofilm, fitted by a sum of two exponentials, roughly corresponding to the base and vertical stages of the biofilm (*SI Appendix*, Fig. S3*D*). The biofilm density at given height and point in time is then modeled as $d(t, h) = d_f(h)/1 + \exp(-m(h)(t - t_h(h)))$, where $t_h(h) = c_{t0} + c_{t1}\ h$ is the time to reach height h, $m(h) = c_{m0} + c_{m1}\ h$ is the speed of maturation, and $d_f(h) = c_{d1}e^{c_{d2}h} + c_{d3}e^{c_{d4}h} + c_{d0}$ the final biomass density (*SI Appendix*, Fig. S3*E*), with parameters given in *SI Appendix*, Table S2.

Estimation of oxygen concentration. Here we model oxygen concentration throughout the liquid phase containing the biofilm to fit data from an oxygen sensor, which are only available at depths above the biofilm. Oxygen enters the liquid phase at its interface with the air phase, which is kept in equilibrium. Oxygen then diffuses down the liquid phase and is consumed by the biofilm at the bottom. We use a one-dimensional reaction–diffusion model, assuming that oxygen concentration varies by height, without significant horizontal gradients. We use a variable diffusion coefficient for oxygen in the liquid phase to account for mixing due to convection and we use variable oxygen consumption per biomass density to account for changes in metabolic state through the biofilm due to hypoxia.

Oxygen diffusion. The experimental setup is kept covered with a lid, so consumption of oxygen by the biofilm reduces its availability in the air phase during the experiment. We therefore consider an oxygen concentration at the interface of the liquid phase o_{surf} lower than the expected o_{sat} in an open environment. Data from the oxygen sensor shows that oxygen concentration in a region between the liquid surface and the top of the biofilm remains constant at an intermediate level, suggesting that there is mixing of the liquid phase where the lack of surface tension allows for convection (65). We model this as an effective increase in the diffusion coefficient of oxygen in water from D_{oxy} to D_{eff} at intermediate depths, between the surface and the top of the biofilm (*SI Appendix*, Fig. S4*A*). Therefore, the concentration of oxygen varies as $\frac{d\,o(t,h)}{dt} = D(t,h)\frac{d^2\,o(t,h)}{dh^2} + \frac{d\,D(t,h)}{dh}\frac{d\,o(t,h)}{dh} - C(t,h)$, where $o(t,h)$ represents the oxygen concentration at time t and height h, $D(t,h)$ is the variable diffusion coefficient, and $C(t,h)$ is the consumption of oxygen (discussed below and shown in *SI Appendix*, Table S2).

Oxygen consumption. At densities below 0.35 by volume, the biofilm is sparse enough not to block the diffusion of oxygen molecules through the liquid. The typical distance between hyphae in the biofilm is in the order of 20 μm to 50 μm (as measured from microscopy images), which allows rapid horizontal diffusion and prevents the creation of large-scale horizontal gradients in oxygen concentration. We then model oxygen consumption at a given height as proportional to the local biomass density and dependent in the local oxygen concentration. We estimate that oxygen consumption is reduced when oxygen concentration falls below a threshold o_{thresh} and cells enter a hypoxic metabolic state (41, 66) (*SI Appendix*, Fig. S4 *B* and *C*). Therefore, oxygen consumption is $C(t,h) = c(o(t,h))d(t,h)$, where $d(t,h)$ is the biomass density and $c(o)$ is the oxygen consumption per biomass density (*SI Appendix*, Table S2).

Numerical simulation. We simulate the reaction–diffusion model using the Crank–Nicolson method (67) for the 24-h period until the biofilm reaches maturity. We choose time steps and distance increments such that $\Delta t < 0.5\ \Delta h^2/D$, guaranteeing the stability of the solution. The model shows hypoxic zones as the biofilm starts to become denser at around 14 h and anoxic zones at the base of the biofilm as it approaches maturity (*SI Appendix*, Fig. S4*D*). Parameters were optimized to best fit the data from the oxygen sensor and are summarized in *SI Appendix*, Table S2.

Flow Cytometry Reporter Characterization.

$_p$erg25A-GFP reporter. Conidia of AF293 (no fluorophore) or *$_p$erg25A-GFP* were swollen in GMM broth supplemented with 0.5% yeast extract (210929; Gibco) at 10^6 conidia per mL for 5 h at 37 °C and 100 rpm agitation. The AF293 swollen conidia were analyzed from 21% O_2 after 5 h. The *$_p$erg25A-GFP* swollen conidia were analyzed from 21% O_2 after 5 h (0 min hypoxia) or after additional incubation at 0.2% O_2 (hypoxia) for the noted time. The population was gated for cells that were singlets and swollen and analyzed for GFP/FTIC signal (488 nm) using a Guava easyCyte 8HT benchtop flow cytometer. Data were analyzed using FlowJo v.9.9.6.

$_p$xylP-GFP reporter. Conidia of AF293 (no reporter system) or *$_p$xylP-GFP* were swollen as described above. The swollen conidia were washed once with 1× PBS and resuspended in 4% xylose in minimal media (GMM without 1% glucose) for the times as noted. The populations were gated for cells that were singlets and swollen and were analyzed for GFP/FITC (488 nm) using a MacsQuant VYB flow cytometer. Data were analyzed using FlowJo v9.9.6.

Statistics. Unless otherwise noted, statistics were performed in GraphPad Prism 8. Unless otherwise noted, comparisons for $n = 2$ utilized a Student's unpaired two-tailed t test and comparisons for $n > 3$ utilized a one-way ANOVA with a Tukey's multiple comparisons test. Fluorescent micrographs and three-dimensional (3D) renderings were prepared from representative samples of three to five biological replicates. Heat maps display data from the representative sample of three replicates.

Data Availability. All study data are included in the paper and *SI Appendix*.

ACKNOWLEDGMENTS. We thank M. Lionakis (NIH) and A. Kline (NIH) for sharing the *S. apiospermum* isolate, and A. Lavanway (Dartmouth) for their microscopy expertise. We thank Drs. Aaron Mitchell, Damian Krysan, and George O'Toole for constructive critiques of the data. This work was supported by the efforts of R.A.C. through funding by NIH National Institute of Allergy and Infectious Diseases (NIAID) (Grants R01AI130128 and R01AI146121). R.A.C. holds an Investigators in Pathogenesis of Infectious Diseases Award from the Burroughs Wellcome Fund. C.H.K. was supported by the NIH NIAID Ruth L. Kirschstein National Research Service Award (F31AI138354). C.D.N. is

supported by NSF Molecular and Cellular Biosciences 1817342, a Burke Award from Dartmouth College, a pilot award from the Cystic Fibrosis Foundation (STANTO15RO), NIH Grant P30-DK117469, and NIH Grant P20-GM113132 to the Dartmouth BioMT Center of Biomedical Research Excellence.

1. N. P. Wiederhold, Antifungal resistance: Current trends and future strategies to combat. *Infect. Drug Resist.* **10**, 249–259 (2017).
2. M. Frieri, K. Kumar, A. Boutin, Antibiotic resistance. *J. Infect. Public Health* **10**, 369–378 (2017).
3. R. M. Humphries *et al*., CLSI methods development and standardization working group best practices for evaluation of antimicrobial susceptibility tests. *J. Clin. Microbiol.* **56**, e01934-17 (2018).
4. P. J. Paterson, S. Seaton, H. G. Prentice, C. C. Kibbler, Treatment failure in invasive aspergillosis: Susceptibility of deep tissue isolates following treatment with amphotericin B. *J. Antimicrob. Chemother.* **52**, 873–876 (2003).
5. E. M. Johnson *et al*., Lack of correlation of in vitro amphotericin B susceptibility testing with outcome in a murine model of Aspergillus infection. *J. Antimicrob. Chemother.* **45**, 85–93 (2000).
6. N. Kartsonis *et al*., Caspofungin susceptibility testing of isolates from patients with esophageal candidiasis or invasive candidiasis: Relationship of MIC to treatment outcome. *Antimicrob. Agents Chemother.* **49**, 3616–3623 (2005).
7. L. Rojas *et al*., Vancomycin MICs do not predict the outcome of methicillin-resistant Staphylococcus aureus bloodstream infections in correctly treated patients. *J. Antimicrob. Chemother.* **67**, 1760–1768 (2012).
8. G. Orazi, G. A. O'Toole, "It takes a village": Mechanisms underlying antimicrobial recalcitrance of polymicrobial biofilms. *J. Bacteriol.* **202**, e00530-19 (2019).
9. J. Berman, D. J. Krysan, Drug resistance and tolerance in fungi. *Nat. Rev. Microbiol.* **18**, 319–331 (2020).
10. C. W. Hall, T. F. Mah, Molecular mechanisms of biofilm-based antibiotic resistance and tolerance in pathogenic bacteria. *FEMS Microbiol. Rev.* **41**, 276–301 (2017).
11. T. F. Mah, G. A. O'Toole, Mechanisms of biofilm resistance to antimicrobial agents. *Trends Microbiol.* **9**, 34–39 (2001).
12. R. Bojsen, B. Regenberg, A. Folkesson, Saccharomyces cerevisiae biofilm tolerance towards systemic antifungals depends on growth phase. *BMC Microbiol.* **14**, 305 (2014).
13. M. D. LaFleur, C. A. Kumamoto, K. Lewis, Candida albicans biofilms produce antifungal-tolerant persister cells. *Antimicrob. Agents Chemother.* **50**, 3839–3846 (2006).
14. L. R. Martinez, A. Casadevall, Susceptibility of Cryptococcus neoformans biofilms to antifungal agents in vitro. *Antimicrob. Agents Chemother.* **50**, 1021–1033 (2006).
15. R. Bojsen, B. Regenberg, A. Folkesson, Persistence and drug tolerance in pathogenic yeast. *Curr. Genet.* **63**, 19–22 (2017).
16. M. J. Seidler, S. Salvenmoser, F. M. Müller, Aspergillus fumigatus forms biofilms with reduced antifungal drug susceptibility on bronchial epithelial cells. *Antimicrob. Agents Chemother.* **52**, 4130–4136 (2008).
17. M. W. Harding, L. L. Marques, R. J. Howard, M. E. Olson, Can filamentous fungi form biofilms? *Trends Microbiol.* **17**, 475–480 (2009).
18. W. C. Chiang *et al*., Extracellular DNA shields against aminoglycosides in Pseudomonas aeruginosa biofilms. *Antimicrob. Agents Chemother.* **57**, 2352–2361 (2013).
19. J. Nett *et al*., Putative role of beta-1,3 glucans in Candida albicans biofilm resistance. *Antimicrob. Agents Chemother.* **51**, 510–520 (2007).
20. R. Rajendran *et al*., Extracellular DNA release acts as an antifungal resistance mechanism in mature Aspergillus fumigatus biofilms. *Eukaryot. Cell* **12**, 420–429 (2013).
21. B. S. Tseng *et al*., The extracellular matrix protects Pseudomonas aeruginosa biofilms by limiting the penetration of tobramycin. *Environ. Microbiol.* **15**, 2865–2878 (2013).
22. T. R. De Kievit *et al*., Multidrug efflux pumps: Expression patterns and contribution to antibiotic resistance in Pseudomonas aeruginosa biofilms. *Antimicrob. Agents Chemother.* **45**, 1761–1770 (2001).
23. P. K. Mukherjee, J. Chandra, D. M. Kuhn, M. A. Ghannoum, Mechanism of fluconazole resistance in Candida albicans biofilms: Phase-specific role of efflux pumps and membrane sterols. *Infect. Immun.* **71**, 4333–4340 (2003).
24. R. Rajendran *et al*., Azole resistance of Aspergillus fumigatus biofilms is partly associated with efflux pump activity. *Antimicrob. Agents Chemother.* **55**, 2092–2097 (2011).
25. G. Ramage, S. Bachmann, T. F. Patterson, B. L. Wickes, J. L. López-Ribot, Investigation of multidrug efflux pumps in relation to fluconazole resistance in Candida albicans biofilms. *J. Antimicrob. Chemother.* **49**, 973–980 (2002).
26. B. Schaible, C. T. Taylor, K. Schaffer, Hypoxia increases antibiotic resistance in Pseudomonas aeruginosa through altering the composition of multidrug efflux pumps. *Antimicrob. Agents Chemother.* **56**, 2114–2118 (2012).
27. D. Nguyen *et al*., Active starvation responses mediate antibiotic tolerance in biofilms and nutrient-limited bacteria. *Science* **334**, 982–986 (2011).
28. G. Borriello, L. Richards, G. D. Ehrlich, P. S. Stewart, Arginine or nitrate enhances antibiotic susceptibility of Pseudomonas aeruginosa in biofilms. *Antimicrob. Agents Chemother.* **50**, 382–384 (2006).
29. J. V. Desai, A. P. Mitchell, D. R. Andes, Fungal biofilms, drug resistance, and recurrent infection. *Cold Spring Harb. Perspect. Med.* **4**, a019729 (2014).
30. C. H. Kowalski *et al*., Fungal biofilm morphology impacts hypoxia fitness and disease progression. *Nat. Microbiol.* **4**, 2430–2441 (2019).
31. T. Rossignol *et al*., Correlation between biofilm formation and the hypoxic response in Candida parapsilosis. *Eukaryot. Cell* **8**, 550–559 (2009).
32. V. C. Thomas, P. D. Fey, Take my breath away. *eLife* **6**, e25739 (2017).
33. C. Stichternoth, J. F. Ernst, Hypoxic adaptation by Efg1 regulates biofilm formation by Candida albicans. *Appl. Environ. Microbiol.* **75**, 3663–3672 (2009).
34. K. S. Williamson *et al*., Heterogeneity in Pseudomonas aeruginosa biofilms includes expression of ribosome hibernation factors in the antibiotic-tolerant subpopulation and hypoxia-induced stress response in the metabolically active population. *J. Bacteriol.* **194**, 2062–2073 (2012).
35. J. N. Anderl, J. Zahller, F. Roe, P. S. Stewart, Role of nutrient limitation and stationary-phase existence in Klebsiella pneumoniae biofilm resistance to ampicillin and ciprofloxacin. *Antimicrob. Agents Chemother.* **47**, 1251–1256 (2003).
36. P. S. Stewart *et al*., Reaction-diffusion theory explains hypoxia and heterogeneous growth within microbial biofilms associated with chronic infections. *NPJ Biofilms Microbiomes* **2**, 16012 (2016).
37. G. Borriello *et al*., Oxygen limitation contributes to antibiotic tolerance of Pseudomonas aeruginosa in biofilms. *Antimicrob. Agents Chemother.* **48**, 2659–2664 (2004).
38. M. C. Walters 3rd, F. Roe, A. Bugnicourt, M. J. Franklin, P. S. Stewart, Contributions of antibiotic penetration, oxygen limitation, and low metabolic activity to tolerance of Pseudomonas aeruginosa biofilms to ciprofloxacin and tobramycin. *Antimicrob. Agents Chemother.* **47**, 317–323 (2003).
39. E. Werner *et al*., Stratified growth in Pseudomonas aeruginosa biofilms. *Appl. Environ. Microbiol.* **70**, 6188–6196 (2004).
40. J. E. Nett, K. Crawford, K. Marchillo, D. R. Andes, Role of Fks1p and matrix glucan in Candida albicans biofilm resistance to an echinocandin, pyrimidine, and polyene. *Antimicrob. Agents Chemother.* **54**, 3505–3508 (2010).
41. N. Grahl, T. M. Dinamarco, S. D. Willger, G. H. Goldman, R. A. Cramer, Aspergillus fumigatus mitochondrial electron transport chain mediates oxidative stress homeostasis, hypoxia responses and fungal pathogenesis. *Mol. Microbiol.* **84**, 383–399 (2012).
42. D. Chung *et al*., ChIP-seq and in vivo transcriptome analyses of the Aspergillus fumigatus SREBP SrbA reveals a new regulator of the fungal hypoxia response and virulence. *PLoS Pathog.* **10**, e1004487 (2014).
43. S. D. Willger *et al*., A sterol-regulatory element binding protein is required for cell polarity, hypoxia adaptation, azole drug resistance, and virulence in Aspergillus fumigatus. *PLoS Pathog.* **4**, e1000200 (2008).
44. D. Vordermark, T. Shibata, J. M. Brown, Green fluorescent protein is a suitable reporter of tumor hypoxia despite an oxygen requirement for chromophore formation. *Neoplasia* **3**, 527–534 (2001).
45. I. Zadra, B. Abt, W. Parson, H. Haas, xylP promoter-based expression system and its use for antisense downregulation of the Penicillium chrysogenum nitrogen regulator NRE. *Appl. Environ. Microbiol.* **66**, 4810–4816 (2000).
46. A. Rosenberg *et al*., Antifungal tolerance is a subpopulation effect distinct from resistance and is associated with persistent candidemia. *Nat. Commun.* **9**, 2470 (2018).
47. N. Grahl *et al*., In vivo hypoxia and a fungal alcohol dehydrogenase influence the pathogenesis of invasive pulmonary aspergillosis. *PLoS Pathog.* **7**, e1002145 (2011).
48. N. Shukla, A. H. Osmani, S. A. Osmani, Microtubules are reversibly depolymerized in response to changing gaseous microenvironments within *Aspergillus nidulans* biofilms. *Mol. Biol. Cell* **28**, 634–644 (2017).
49. D. K. Morales *et al*., Control of Candida albicans metabolism and biofilm formation by Pseudomonas aeruginosa phenazines. *MBio* **4**, e00526-12 (2013).
50. C. Mateus, S. A. Crow Jr., D. G. Ahearn, Adherence of Candida albicans to silicone induces immediate enhanced tolerance to fluconazole. *Antimicrob. Agents Chemother.* **48**, 3358–3366 (2004).
51. K. M. Yeater *et al*., Temporal analysis of Candida albicans gene expression during biofilm development. *Microbiology* **153**, 2373–2385 (2007).
52. C. A. Kumamoto, A contact-activated kinase signals Candida albicans invasive growth and biofilm development. *Proc. Natl. Acad. Sci. U.S.A.* **102**, 5576–5581 (2005).
53. I. Denega, C. d'Enfert, S. Bachellier-Bassi, *Candida albicans* biofilms are generally devoid of persister cells. *Antimicrob. Agents Chemother.* **63**, e01979-18 (2019).
54. C. J. Nobile *et al*., A recently evolved transcriptional network controls biofilm development in Candida albicans. *Cell* **148**, 126–138 (2012).
55. J. E. Nett, A. J. Lepak, K. Marchillo, D. R. Andes, Time course global gene expression analysis of an in vivo Candida biofilm. *J. Infect. Dis.* **200**, 307–313 (2009).

56. U. Binder, E. Maurer, M. Lackner, C. Lass-Flörl, Effect of reduced oxygen on the antifungal susceptibility of clinically relevant aspergilli. *Antimicrob. Agents Chemother.* **59**, 1806–1810 (2015).
57. P. A. Warn, A. Sharp, J. Guinea, D. W. Denning, Effect of hypoxic conditions on in vitro susceptibility testing of amphotericin B, itraconazole and micafungin against Aspergillus and Candida. *J. Antimicrob. Chemother.* **53**, 743–749 (2004).
58. Y. Li *et al*., Mitochondrial dysfunctions trigger the calcium signaling-dependent fungal multidrug resistance. *Proc. Natl. Acad. Sci. U.S.A.* **117**, 1711–1721 (2020).
59. S. Dhingra, J. C. Buckey, R. A. Cramer, Hyperbaric oxygen reduces Aspergillus fumigatus proliferation *in vitro* and influences *in vivo* disease outcomes. *Antimicrob. Agents Chemother.* **62**, e01953-17 (2018).
60. M. A. Spero, D. K. Newman, Chlorate specifically targets oxidant-starved, antibiotic-tolerant populations of Pseudomonas aeruginosa biofilms. *MBio* **9**, e01400-18 (2018).
61. E. Y. Basenko *et al*., FungiDB: An integrated bioinformatic resource for Fungi and oomycetes. *J. Fungi (Basel)* **4**, 39 (2018).
62. T. Kubodera, N. Yamashita, A. Nishimura, Transformation of Aspergillus sp. and Trichoderma reesei using the pyrithiamine resistance gene (ptrA) of Aspergillus oryzae. *Biosci. Biotechnol. Biochem.* **66**, 404–406 (2002).
63. P. J. Punt, R. P. Oliver, M. A. Dingemanse, P. H. Pouwels, C. A. van den Hondel, Transformation of Aspergillus based on the hygromycin B resistance marker from Escherichia coli. *Gene* **56**, 117–124 (1987).
64. R. Hartmann *et al*., BiofilmQ, a software tool for quantitative image analysis of microbial biofilm communities. bioRxiv:10.1101/735423 (15 August 2019).
65. L. Rongy, K. B. Haugen, A. Firoozabadi, Mixing from Fickian diffusion and natural convection in binary non-equilibrium fluid phases. *AIChE J.* **58**, 1336–1345 (2012).
66. A. Taubitz, B. Bauer, J. Heesemann, F. Ebel, Role of respiration in the germination process of the pathogenic mold Aspergillus fumigatus. *Curr. Microbiol.* **54**, 354–360 (2007).
67. J. Crank, P. Nicolson, A practical method for numerical evaluation of solutions of partial differential equations of the heat-conduction type. *Proc. Camb. Philos. Soc.* **43**, 50–67 (1947).